Photoacoustics 28 (2022) 100419

Contents lists available at ScienceDirect

Photoacoustics

journal homepage: www.elsevier.com/locate/pacs

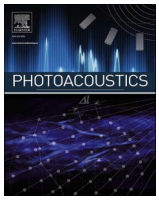

Ultrasensitive broadband photoacoustic microscopy based on common-path interferometric surface plasmon resonance sensing

Wei Song *, Yushu Dong, Youxian Shan, Fan Yang, Changjun Min, Xiaocong Yuan *

Nanophotonics Research Center, Shenzhen Key Laboratory of Micro-Scale Optical Information Technology, Institute of Microscale Optoelectronics, Shenzhen University, Shenzhen 518060, China

A B S T R A C T

Ultrafast and sensitive response of surface plasmon polaritons to the ultrasonically-modulated changes in refractive index of the water allows photoacoustic impulses to be measured using surface plasmon resonance (SPR) sensors. However, the sensing modalities always suffer from either low sensitivity or instable signal output, possibly precluding imaging recovery. By exploiting that pressure transients can substantially produce phase shift in *p*-polarized optical reflection but have no impact on *s*-polarized component in SPR sensing, we develop a common-path interferometric SPR sensor for photoacoustic measurement, in which time-varying light interference between photoacoustically-perturbed *p*-polarized beam and its orthogonal *s*-polarized component of a single interrogation laser is monitored. Such configuration retains optimum photoacoustic measurement with concurrent very stable signal output, high sensitivity (noise-equivalent-pressure sensitivity of ~95.6 Pa), and broad bandwidth (~173 MHz). Volumetric microvascular imaging from mouse ear in vivo is obtained, suggesting that the novel sensing approach potentially advances biomedical photoacoustic applications.

1. Introduction

Photoacoustic imaging technology is capable of mapping optical absorption distribution directly by acoustically detecting pressure waves (i.e. photoacoustic signals) from the transient thermo-elastic expansion as a result of biomolecule's absorption of the pulsed laser energy [1,2]. Capturing the molecular specificity of nonfluorescent intrinsic chromophores, such as hemoglobin, DNA/RNA, and lipids, enables the technology studying physiopathology label-freely, including vascular anatomy, tumor metastasis, and brain activities [3–7]. Optical-resolution photoacoustic microscopy (OR-PAM), a unique implementation of photoacoustic imaging, realizes lateral resolution down to micrometer and even sub-micrometer by focusing photoacoustic illumination with an optical objective [1–7], which specifically accommodates to observing biological processes at cellular and subcellular scales. Therefore, OR-PAM complements the well-established pure optical microscopic techniques (e.g., multiphoton microscopy, optical coherence tomography) that predominantly rely on optical scattering, fluorescence, or polarization for the imaging contrast [8–10].

Reconstructing biomedical photoacoustic images requires accurate response to the pressure transients in terms of both amplitude and spectrum. The photoacoustic signal amplitude is proportional to the optical absorption coefficient and local optical fluence, delineating the optical absorption distribution within biological samples [1–3]. Sufficient imaging signal-to-noise ratio (SNR) requires highly sensitive acoustic detection, which assures the microscopic structures of the chromophores with low-level optical absorption or at large depth to be discerned. The resolving capability along the depth direction (i.e., axial resolution) is predominantly determined by the ultrasonic detector's bandwidth [11]. Broadband frequency response of the ultrasonic detector permits reliable reconstruction of the photoacoustic volumetric image, thereby offering accurate depth estimation of chromophores. So far, piezoelectric transducers are widely employed for detecting the photoacoustic waves because of their accessibility and low cost [11]. Yet, they possibly fail to respond the photoacoustic transients because of inadequate detection sensitivity over broad spectral band arising from the inherent physical property of the piezoelectric materials. This usually causes poor depth resolution in the conventional OR-PAM setups, and thus the photoacoustic volumetric imaging is compromised because of severely distorted imaging voxels [4,5,7].

Optical technologies of ultrasound detection emerge as promising alternatives to the piezoelectric-dominated landscape [12,13]. By interrogating the acoustically modulated optical resonance and/or optical reflectance, the optical sensing approaches, such as plano-concave optical microresonator, optomechanical ultrasound sensor, and Fabry–Perot interferometer, are capable of detecting ultrasounds at very high sensitivity [14–16]. Whereas, the depth resolution in the photoacoustic volumetric imaging is often unsatisfactory due to the

* Corresponding authors.
E-mail addresses: weisong@szu.edu.cn (W. Song), xcyuan@szu.edu.cn (X. Yuan).

https://doi.org/10.1016/j.pacs.2022.100419
Received 17 April 2022; Received in revised form 15 September 2022; Accepted 24 October 2022
Available online 25 October 2022

bandwidth confined at a few tens of megahertz. High-frequency ultrasound can be captured by optical micro-ring resonator [17,18], but the detector requires time-consuming fabrication procedures with low yield. Silicon-on-insulator resonator possesses an ultrawide detection bandwidth [19], which, however, is in practice difficult for imaging thick biological specimens or in vivo imaging because its working distance is limited to around several tens of micrometers.

Recently, optical sensing modality based on surface plasmon resonance (SPR), which has been adopted in a wide range of label-free biosensing of molecules in their natural form and molecular interaction [20–23], is translated to ultrasound detection [24–27]. The SPR sensor fabrication is simply accomplished by depositing a commercially available metal film onto the dielectric surface (e.g., a prism or a coverslip). Ultrafast temporal dynamics and strongly localized evanescent field of surface plasmon polaritons (SPPs) enables broadband frequency response (>170 MHz) in the SPR sensors [27,28]. Strikingly, on basis of the fact that the phase shift is extremely sensitive to the variations in refractive index near the interface of the metal and water [21–23], phase-shifted SPR sensor demonstrates significant sensitivity improvement in photoacoustic measurement [29]. However, because the initial phase of the interrogating beam fluctuates randomly (having a phase drift of $\geq 6.6 \times 10^{-3}$ rad) due to ambient disturbances [23], it is very challenging that such sensing approach maintains the optimum sensitivity for acquiring the photoacoustic signals [29], possibly compromising the imaging recovery. In this work, we propose a common-path interferometric SPR sensor for achieving a faithful representation of the photoacoustic signals. It is proved that, in the SPR sensing, the phase of the *p*-polarized interrogation light is extremely sensitive to ultrasonic perturbations but that of the *s* polarization is independent of ultrasounds [20–27]. When applying one single interrogation beam (i.e., consisting of the *p*- and *s*-polarization components), the phase difference between the two orthogonally polarized components is immune to the surrounding disturbances because they travel through the completely same optical path. Consequently, by monitoring temporally-varying light interference between ultrasonically-perturbed *p*-polarized component and invariant *s*-polarized component, the photoacoustic measurement is stabilized effectively with superior sensitivity and broad bandwidth, which effectively eliminates the inevitable noises from the phase fluctuations in the phase-shifted SPR sensor [29]. Moreover, our sensor exploits highly-sensitive phase shift for responding the photoacoustic impulses [21–23], so its detection sensitivity remarkably surpasses those polarization-based SPR sensing technologies by interrogating the light reflectivity while still persisting broadband frequency response [25–27]. We acquired the volumetric images from both phantom and mouse ear in vivo with an OR-PAM system incorporating the novel sensor.

2. Materials and methods

2.1. Principle of the common-path interferometric SPR sensor

The operating mechanism of the common-path interferometric SPR sensor is shown in Fig. 1(a). An interrogation beam consisting of orthogonally *p*- and *s*-polarized components is incident on the Au film across the prism (Fig. 1(a)). A fraction of the incident energy of the *p*-polarized component contributes to the SPPs formation at the Au-water interface, and then is reflected in the total reflection region [20]. The complex optical field reflectivity, $r_p = |r_p|e^{i\varphi_p}$, depends on the incidence angle (θ) and refractive index of the water (n_w), where $|r_p|$ is the amplitude reflectivity and φ_p is the phase (Note 1 in Supplementary materials). As θ and n_w varying, an abrupt phase transition takes place in the reflected *p*-polarized light (Fig. 1(b)). For the *s*-polarized component, the complex optical field reflectivity is expressed as $r_s = |r_s|e^{i\varphi_s}$ (Note 2 in Supplementary materials), where its amplitude reflectivity ($|r_s|$) and phase (φ_s) are independent of θ and n_w (Fig. 1(b)) because of no contribution to the excitation of SPPs [20].

The incidence angle θ is fixed during photoacoustic/ultrasonic detection [29]. Laser-induced ultrasonic pressure (P) causes a time-varying change in n_w, thereby modulating the SPPs. Accordingly, a phase shift ($\Delta\varphi_p(P)$) is produced in the reflected *p*-polarized component

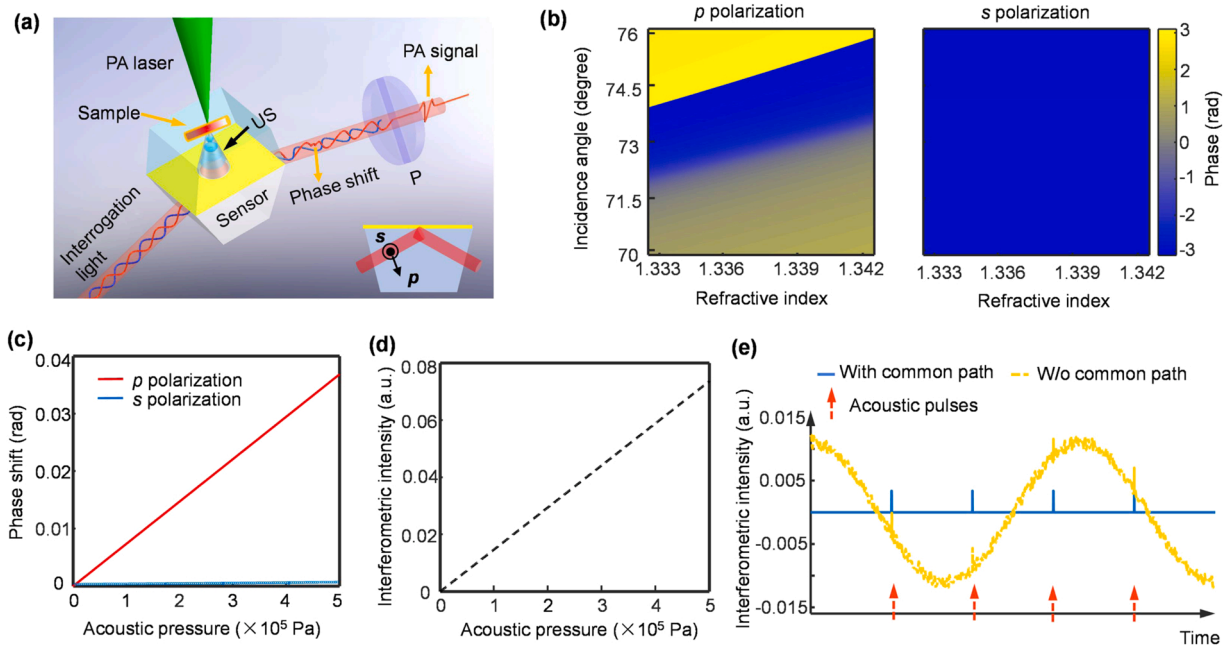

Fig. 1. Working principle of the common-path interferometric SPR sensor. (a) Schematic representation of the sensor in response to laser-induced ultrasound, where the polarization directions of *s*- and *p*-polarized components are displayed in lower right corner. P: polarizer; PA: photoacoustic; US: ultrasound. (b) Phase of the *p*- and *s*-polarized components as a function of the incidence angle and the refractive index of water. (c) Acoustically-modulated phase shifts in the reflected *p*- and *s*-polarized components. (d) Interference intensity of the orthogonally polarized components with respect to the acoustic pressure. (e) Common-path configuration enables the acoustic pulses (with pressure amplitude of 25 kPa) to be retrieved accurately in our sensor (as illustrated by the blue solid line), which suppresses the signal fluctuations (as illustrated by the yellow dotted line) from the phase drifts (with an amplitude of 0.006 rad).[23].

(Fig. 1(c)), leading to its complex optical field reflectivity as

$$r_p(P) = |r_p| e^{i\left(\Delta\varphi_p(P)+\varphi_{p0}(t)\right)} \quad (1)$$

where the initial phase $\varphi_{p0}(t)$ is related to the surrounding disturbances without the ultrasonic perturbation (with the frequency less than hundreds of Hz), varying much slower compared with the ultrasonic pressure transient (usually tens of MHz) [21–23]. Thus, the concise expressions of P and $\Delta\varphi_p(P)$ are presented in Eq. (1) to highlight the impact of the phase fluctuation $\varphi_{p0}(t)$ on the detection stability in the sensor. Because the phase of the reflected beam in the SPR sensing is much more sensitive than the amplitude reflectivity to variations in n_w (Fig. S2 in Supplementary materials) [21–24], ultrasonically-perturbed change in $|r_p|$ is very slight. Thus, we reasonably consider $|r_p|$ unchanged during pressure measurement. Correspondingly, the optical reflection field is given as

$$E_p(P) = r_p(P)E_{p0} = A_p e^{i\left(\Delta\varphi_p(P)+\varphi_{p0}(t)\right)} \quad (2)$$

where E_{p0} is the incident optical field, and $A_p = E_{p0}|r_p|$ is the amplitude of the reflected p-polarized component. The s-polarized reflection is irrespective of the ultrasonic perturbations (i.e., $\Delta\varphi_s(P) \approx 0$ in Fig. 1(c)), and its complex optical field reflectivity is expressed as

$$r_s(P) = |r_s| e^{i(\varphi_{s0}(t))} \quad (3)$$

where its initial phase $\varphi_{s0}(t)$ is impacted by the ambient conditions, analogue to the p polarization. We simply derive its optical reflection field as $E_s(P) = A_s e^{i(\varphi_{s0}(t))}$, where $A_s = E_{s0}|r_s|$ represents the amplitude with an incident optical field E_{s0}.

By recombining the orthogonally-polarized reflection beams using a polarizer (P in Fig. 1(a)), light interference occurs at the transmission direction of the polarizer, which is characterized as

$$I(P) = A_p^2 sin^2\alpha + A_s^2 cos^2\alpha + A_p A_s sin2\alpha \cos(\Delta\varphi_p(P) + \Delta\Phi(t)) \quad (4)$$

where α is the angle of the s-polarized component relative to the polarizer's transmission direction, and $\Delta\Phi(t) = \varphi_{p0}(t) - \varphi_{s0}(t)$ represents the initial phase difference between the two polarized components without exerting ultrasounds. Because the amplitude reflectivity ($|r_p|$) in response to the pressure perturbation is remarkably weaker compared with the phase (Fig. S2 in Supplementary materials) [21–24], A_p is considered constant during ultrasonic detection. From Eq. (4), we conclude that the ultrasonically-modulated light interference intensity depends on both the phase shift ($\Delta\varphi_p(P)$) and the initial phase difference ($\Delta\Phi(t)$).

In our common-path interferometric SPR sensing technology (Fig. 1(a)), the orthogonally p- and s-polarized components always travel through the same optical path, so $\Delta\Phi(t)$ remains constant. According to Eq. (4), the interference intensity solely depends on the ultrasonically-modulated phase shift ($\Delta\varphi_p(P)$), indicating that monitoring the interferometric intensity allows the photoacoustic pressure to be measured (Fig. 1(d)). Although the previously-developed phase-shifted SPR sensor is also based on the phase interrogation [29], capturing the interferometric intensity using a Mach–Zehnder interferometer (MZI) is very vulnerable to the surrounding disturbances, thereby suffering from severe drifts in $\Delta\Phi(t)$ [23]. The interferometric intensity fluctuates due to the phase noises (as illustrated by yellow dotted line in Fig. 1(e)), which generates an inaccurate photoacoustic measurement. In contrast, by maintaining $\Delta\Phi(t)$ with the common-path interferometric configuration, our sensor accesses very stable photoacoustic measurement (as illustrated by blue line in Fig. 1(e)). In the future, we plan to optimize the theoretical modal for more accurately characterizing the photoacoustic measurement with a common-path interferometric SPR sensor by considering all noise sources including thermal noise and electric noise.

The frequency response of our sensor relies on the ultrafast dynamics and highly-localized evanescent field of the SPPs, which is essentially identical as the SPR sensors [25–29]. In brief, ultrashort lifetime of the SPPs (approximately hundreds of femtoseconds) in response to ultrasonic perturbations to the evanescent field determines the resulting cutoff ultrasonic frequency at terahertz in theory [28]. Due to remarkably different acoustic impedance between the water and substrate, acoustic waves are reflected from the Au-water interface, leading to an interference between the progressive wave and the acoustic echo. When deconstructive interference occurs within very confined optical penetration region (~185 nm) of the evanescent field, the pressure value equals zero for the ultrasounds at certain frequencies. The cutoff frequency (f_t) can be approximated as $f_t = c/2d$, where c is acoustic speed within the water and d is the field's optical penetration depth. This defines the accessible ultrasonic bandwidth at gigahertz in theory [27]. The finite lateral probing dimensions (having an approximately elliptical structure of ~120 μm along the long axis and ~60 μm along the short axis) in the sensor surface define the ultimate cutoff frequency at hundreds of megahertz [27].

2.2. Development of the common-path interferometric SPR sensor

The common-path interferometric SPR sensor is schematically shown in Fig. 1(a) (Detailed description in Fig. 3(a)). A continuous-wave He-Ne laser (HNL210LB, Thorlabs; 632.8-nm wavelength, 21-mW output power) passing through a polarizer (P, LPVISE100-A, Thorlabs) served as the interrogation light source, defining the coherence length at ~0.2 m in air that is predominantly determined by the laser's linewidth of ~1.5 GHz. A half-wavelength plate (HWP, WPH10M-633, Thorlabs) and quarter-wavelength plate (QWP, WPQ10M-633, Thorlabs) was inserted into the optical path, allowing both the amplitude ratio and initial phase difference between the p- and s-polarized components to be precisely adjusted. The polarized laser output was weakly focused using a lens (f = 125 mm), and then incident on a Kretschmann-type SPR sensor that was fabricated with a layer of Au film (47 nm in thickness) depositing onto the surface of a customized quartz prism (Daheng Optics, China; Its dimension is displayed in Fig. S3 in Supplementary materials). The interrogation light was set at ~72.5° incidence angle, which corresponds to a very steep phase jump (Fig. 1(b)) and thus permits the optimal detection sensitivity. The reflected beam from the Au-water interface passed through a polarizer (Fig. 1(a)). As the optical fields of the p- and s-polarized components projecting at the transmission direction of the polarizer, light interference took place (Eq. 4). In consequence, monitoring the interferometric intensity using a balance photodiode (BD, PDB435a, Thorlabs Inc.) accessed the photoacoustic measurement. Note that a fraction of interrogation light from the laser was deflected to another detector of the BD using a customized beam splitter (BS, Fig. 3(a)) to suppress laser source instability. Distinct from the previously-developed phase-shifted SPR sensor that configured a MZI for light interference [29], our sensor simply utilized one single interrogation beam for realizing the acoustic detection, reducing the hardware complexity obviously. More importantly, such design ensured the common optical travelling path in the orthogonally polarized components, so that the optimum acoustic detection was realized stably by suppressing the phase drifts from the surrounding disturbances (Fig. 1(e)).

2.3. Imaging acquisition of mouse ear in vivo

We performed photoacoustic imaging of the ear microvasculature in vivo in a Swiss Webster mouse (3–5 weeks, weight ~30 g). The animal was anesthetized with a 1.5% gas mixture of isoflurane and oxygen, and immobilized at a home-made stereotaxic mount. After its ear was gently depilated and cleaned with phosphate-buffered saline, we adopted several drops of water between the sensor and the ear skin as the acoustic coupling medium. During imaging, the gas mixture was maintained to minimize motion artifacts. All experimental animal procedures

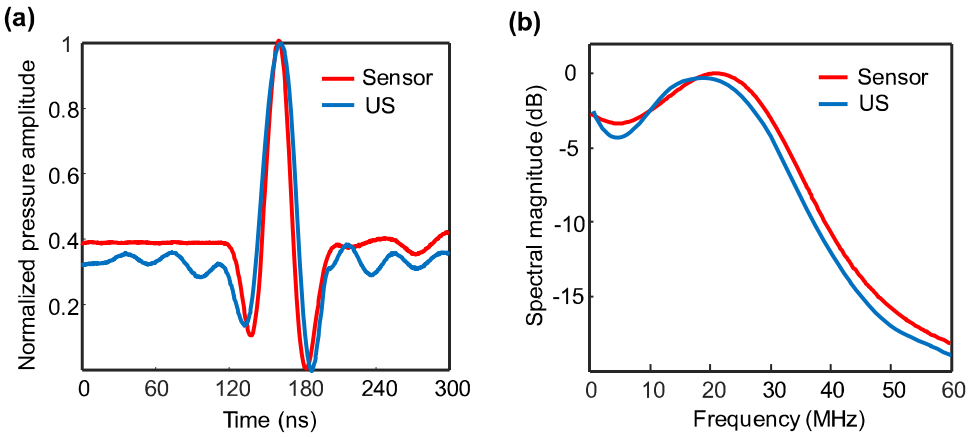

Fig. 2. Ultrasonic response of the sensor. Ultrasonic waveforms (a) and spectra (b) from the sensor and the piezoelectric transducer (US).

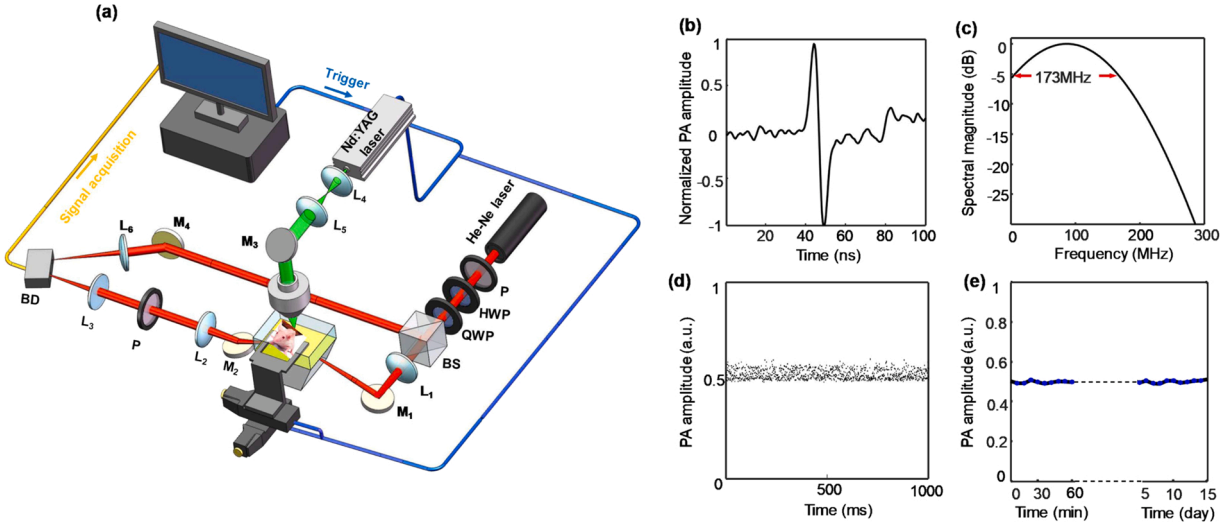

Fig. 3. (a) Schematic illustration of the OR-PAM system incorporating the common-path interferometric SPR sensor. P: polarizer; HWP: half-wavelength plate; QWP: quarter-wavelength plate; L: lens; M: mirror; BD: balance photodiode; BS: beam splitter. Photoacoustic signal from a graphene film in the time (b) and frequency (c) domains. (d) Evaluation of the photoacoustic signal outputs over one second by setting the laser's pulse repetition rate at 1 kHz. (e) Examination of the photoacoustic detection stability of our system for short (~60 min) and long terms (~15 days). PA: photoacoustic.

were conducted in compliance with laboratory animal protocols approved by the Animal Studies Committee of the Shenzhen University.

A field of view (FOV) of 2.5 × 2.5 mm^2 was acquired with a step size of 2.0 μm, taking around 6 min. The photoacoustic excitation laser energy delivered onto the animal skin surface was measured to be ~200 nJ per pulse, which was below the laser safety limit (20 mJ/cm^2) defined by the American National Standards Institute.

3. Results and discussion

3.1. Ultrasonic response of the common-path interferometric SPR sensor

We characterized the ultrasonic response of our sensor using a customized piezoelectric transducer (U20M, NDE technology, Shenzhen) driven by a pulse receiver (5073PR, Olympus Corp.) as the acoustic source. Deionized water was applied between the sensor surface and the transducer for coupling ultrasounds. The ultrasonic signal captured by our sensor is presented in Fig. 2, and the acoustic echo reflected from the water-prism interface was recorded simultaneously. The waveform (Fig. 2(a)) and spectrum (Fig. 2(b)) acquired using our sensor resembled those from the ultrasonic transducer itself, suggesting its accurate response to the ultrasonic excitation. This is in accordance with those SPR-based detectors because the SPPs' response to changes in the water refractive index is essentially responsible for the acoustic detection [25,26].

3.2. Photoacoustic response of the common-path interferometric SPR sensor

We developed an OR-PAM system incorporating a common-path interferometric SPR sensor as the ultrasonic detector (Fig. 3(a)). In brief, a frequency-doubled Nd:YAG laser (SPOT-532, Elforlight Ltd.) with 532-nm wavelength and ~1.2-ns pulse duration served as the photoacoustic illumination source. After collimation with a pair of lenses (L_4 and L_5), the laser output was focused onto the sample by an objective with a numerical aperture (NA) of 0.1. A LabVIEW-programmed interconnect card (PCIe-6321, National Instruments) controlled the firing of the photoacoustic illumination laser, data acquisition (ATS9870, Alazar Tech), and the raster scanning of the motorized stage.

With the OR-PAM system, we studied the sensor's photoacoustic response using a piece of graphene film (~70-nm thickness) as the point source [27]. Time-resolved photoacoustic impulse (Fig. 3b) was recorded with a digital oscilloscope (MDO3104, Tektronix, 1-GHz bandwidth

and 5-GS/s sampling rate), exhibiting a bipolar shape (Fig. S4 in Supplementary materials) as those captured using the optical sensing technologies [12–15]. According to the conversion ratio (~94.4 mV/kPa) of the ultrasonic pressure to the sensor's output voltage that is pre-calibrated using a hydrophone (200-μm-diameter active element, HNP-0200, Onda Corp.), the noise-equivalent-pressure (NEP) sensitivity is estimated at ~95.6 Pa considering the noise level of ~9.0 mV (root-mean-square value), surpassing those SPR-based sensors by interrogating the light reflectivity [25–27]. This is primarily because the ultrasonically-perturbed phase shift is responsible for the photoacoustic measurement in our sensor, which is proved much more sensitive compared with the method based on the light reflectivity [21–23]. The Fourier-transformed power spectrum exhibited a − 6-dB bandwidth of ~173 MHz (Fig. 3(c)), remarkably broader than most conventional OR-PAM systems incorporating a piezoelectric transducer [11].

We examined the detection stability of our sensor by monitoring the photoacoustic amplitudes from a ~180-μm-thick black vinyl over time. By setting a constant-power laser with 1-kHz pulse repetition rate, we recorded the photoacoustic signals within one second. In Fig. 3(d), the peak-to-peak values of signal output over time exhibit a very small signal fluctuation (~5.6%), which is in accordance with the simulations (Fig. 1(e)). Because the initial phase is unpredictable due to the random ambient disturbances [21,23], implementing a complicated compensation is required for stabilizing the signal detection in the phase-shifted SPR sensor [29]. In contrast, $\Delta\Phi(t)$ under static conditions is immune to the vibrations from the surroundings in the common-path interferometric SPR sensor because the orthogonal polarization components travel through the same path. Also, such operation ensures that our sensor remains consistently superior sensitivity in long-term measurement up to one month (Fig. 3(e)). The sensor's excellent performances allow the OR-PAM system for realizing high-fidelity photoacoustic imaging in practical biomedical investigations, for example longitudinal imaging of biological processes in small animals [17].

In Fig. 4(a), the lateral resolution of the OR-PAM system was evaluated by imaging sharp edge of a bar of a USAF-1951 resolution target. The measured photoacoustic amplitudes across the edge were nonlinearly fitted by an error function, giving an estimated lateral resolution of ~3.2 μm according to the line spread function (LSF) derived from the first derivative of the edge spread function (ESF). This agreed with the theoretical diffraction-limited value determined with a 0.1-NA objective and 532-nm illumination wavelength.

The OR-PAM's axial (depth) resolution, which is predominantly determined by the acoustic spectral response of the ultrasonic detector [11], can be quantified by a numerical shift-and-sum simulation assuming two identical photoacoustic point absorbers at different depth separations [18,29]. From the time-shifted waveforms of the two convoluted photoacoustic impulses (Fig. 4(b)), we estimated the axial resolution at ~7.20 μm when two peaks can be differentiated (i.e., with a contrast-to-noise ratio greater than 6 dB as illustrated in the inset of Fig. 4(b)) [18]. Evidently, it represented a good agreement with the theoretically estimated axial resolution (R_a) of ~7.53 μm according to the expression of $R_a = 0.88c/\mathrm{BW}$, where c is the speed of sound in water and BW is the bandwidth [11]. This suggests an excellent sectioning capability of our OR-PAM system offered by the broadband sensor.

3.3. Photoacoustic volumetric imaging of phantom

To demonstrate the volumetric imaging capability of our OR-PAM system, a phantom made from many tungsten filaments with the diameters of 20 μm and 10 μm is imaged in Fig. 5. The maximum-amplitude-projection (MAP) view was reconstructed by projecting the maximum photoacoustic amplitude of each A-line along the depth direction (Fig. 5(a)). All filaments were discernable in the transverse direction due to the system's micrometer-scale lateral resolution. We quantified the average diameters of the thick and thin filaments at 20.14 μm ± 1.25 μm and 10.21 μm ± 0.86 μm, respectively, both of which were consistent with the nominal values. The image SNR was evaluated by defining the noise as the standard deviation of the background without visible samples. For the 10-μm-diameter filaments, the SNR was estimated to be ~31.37 dB; the SNR increased to ~34.23 dB for the 20-μm-diameter tungsten filaments as the thick structure occupied more pixels. Moreover, the depth-resolved features of these randomly-arranged filaments were visible in the volumetric views (Fig. 5(b) and Movie 1 in Supplementary materials), thanks to the good axial resolution from our broadband sensor.

Supplementary material related to this article can be found online at doi:10.1016/j.pacs.2022.100419.

We then evaluated the system's stability during photoacoustic imaging (Fig. 5(c) and (d)). After acquiring the volumetric image of the phantom, repeating B-scan imaging was sequentially implemented by steering the photoacoustic illumination to the lateral position that was approximately highlighted by the white dotted line in Fig. 5(a). Three representative B-scan images (Fig. 5(c)) were color-coded to clearly display their morphological features. Except for comparably good imaging contrast in all B-scan images, the observations represented an evident resemblance among the B-scan images (Fig. 5(c) and Movie 2 in Supplementary materials). The structural similarity index measurement (SSIM) [30], which is a multiplicative combination of the luminance term, the contrast term, and the structural term, was calculated between the first B-scan frame and subsequent each one (Fig. 5(d)). According to the minimum value (>0.94) of the computed SSIMs, we conclude that the common-path interferometric SPR sensor permits for stably capturing the photoacoustic images with superior sensitivity.

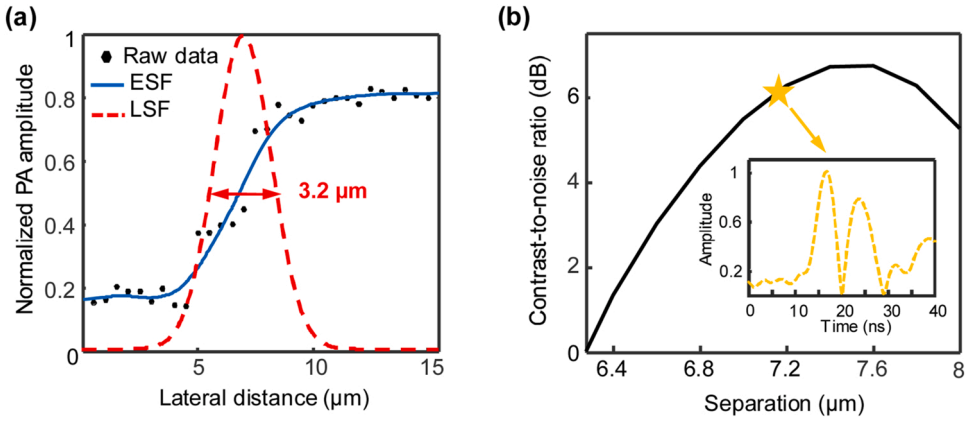

Fig. 4. Determination of the system's spatial resolution. (a) Estimation of the lateral resolution. (b) Axial resolution determined by numerical shift-and-sum simulation, in which the inset shows the signal envelope when the two photoacoustic point sources are positioned at ~7.20-μm separation.

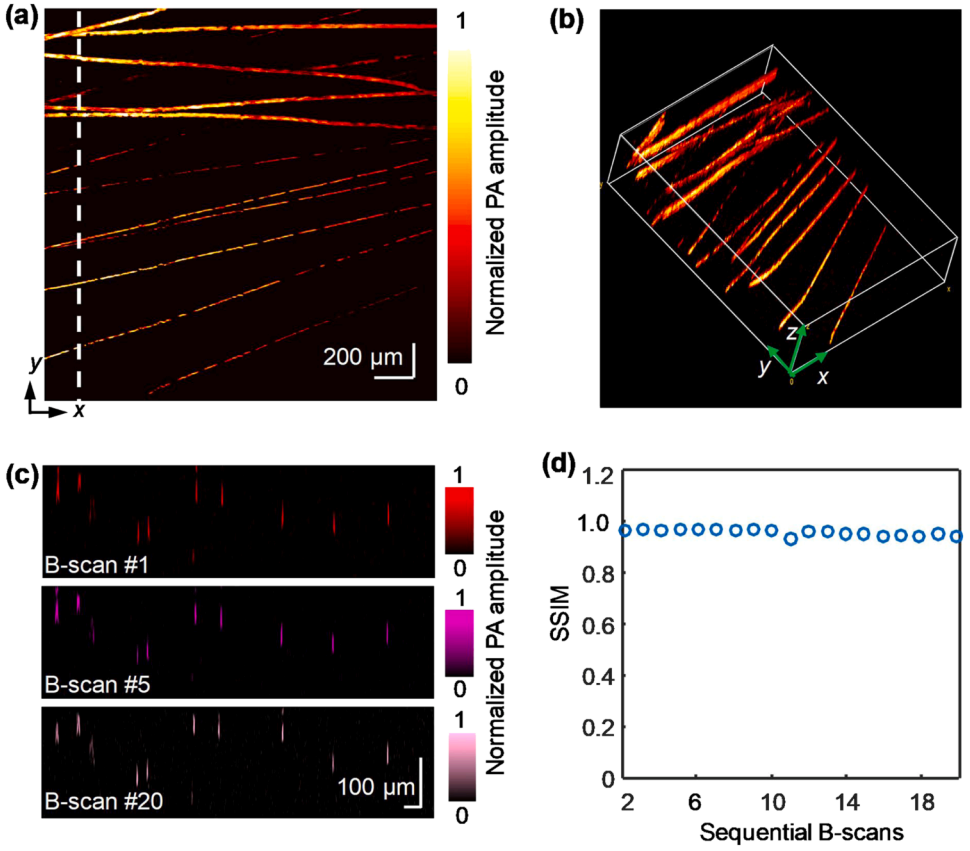

Fig. 5. Maximum-amplitude-projection (a) and volumetric views (b) of a phantom made from many tungsten filaments. Movie 1 (Supplementary materials) provides a volumetric rending from different viewing angles. (c) Three representative B-scan images captured at the same lateral position. Movie 2 (Supplementary materials) shows all cross-sectional images. (d) Structural similarity index measurements (SSIMs) between the first B-scan frame and subsequent each one. The lateral position of the B-scan image was approximately highlighted by the white dotted line in (a). PA: photoacoustic.

Supplementary material related to this article can be found online at doi:10.1016/j.pacs.2022.100419.

3.4. Photoacoustic volumetric imaging of mouse ear in vivo

Label-free microvascular imaging was performed in mouse ear in vivo using the OR-PAM system (Fig. 6). Major blood vessels (Fig. 6(a) and (b)) were observed at the contrast-to-noise ratio (CNR) of ~31.1 dB, where the contrast was defined as the photoacoustic amplitude difference between the vessel and the adjacent background, and the noise was calculated as the standard deviation in the regions without optical absorbers. Besides, densely packed capillaries (with an estimated average diameter of less than 10 μm) was delineated, exhibiting the tortuous anatomical features [31,32]. The observations of the elaborate anatomic characteristics of the microvasculatures primarily benefited from the superior detection sensitivity and micrometer-scale lateral resolution of our OR-PAM system. Note that some discontinuities in the branched microvessels appear, possibly arising from ultrasonic attenuation of the ear cartilage because of transmission-mode imaging operation in the system. One solution is to configure the imaging system at reflection modality by miniaturizing our sensor and integrating it into the central cone of a reflective objective [26].

Supplementary material related to this article can be found online at doi:10.1016/j.pacs.2022.100419.

Spatial microarchitecture of the blood vessels was visualized from the volumetric views (Fig. 6(b) and Movie 3 in Supplementary materials). Good axial resolution of the OR-PAM system, which was predominantly determined by the broadband sensor, allowed visualization of the depth-resolved vascular microanatomy. Otherwise, it is impossible using the conventional OR-PAM systems due to insufficient axial resolution caused by the narrow bandwidth of the piezoelectric transducer [11].

To further evaluate the reliability of the OR-PAM system integrating a common-path interferometric SPR sensor for in vivo photoacoustic applications, the sequential B-scan imaging of mouse ear was implemented by steering the irradiation laser at the same lateral position (highlighted by the white dashed line in Fig. 6(a)). From the cross-sectional views (Fig. 6(c) and Movie 4 in Supplementary materials), the blood vessels were clearly resolved along the depth direction, as discerned in the volumetric views (Fig. 6(b) and Movie 3 in Supplementary materials). More importantly, the B-scan frames captured successively were characterized by visually identical anatomic structures. The averaged SSIM value of ~0.93 (with the minimum value of ~0.91) between the first B-scan frame and subsequent ones (Fig. 6(d)) implied very stable photoacoustic imaging acquisition of the system. In comparison to the phantom's B-scan images, the declined SSIM in in vivo vascular imaging was primarily attributed to the flowing blood across the cross sections of the vasculatures. Still, the substantially large SSIM suggests that our sensor can sensitively detect the photoacoustic impulses from the living biological samples with sufficiently stable response, thus benefiting the practical biomedical photoacoustic applications.

4. Conclusions

The ultrafast temporal response and tightly-localized evanescent field of the SPPs enable measurement of photoacoustic impulses using the SPR sensors through monitoring the laser-induced ultrasonic perturbations to the water refractive index [25–29]. Extremely sensitive to the changes of the refractive index in the phase shift of the optical reflection offers great opportunities of superior sensitivity over a broadband response by interrogating the reflected light phase instead of the light reflectivity in the SPR sensing modalities [22–24]. Unfortunately, random phase drift from the ambient disturbances causes severe signal fluctuations in such SPR sensing [21,29], compromising the photoacoustic measurement.

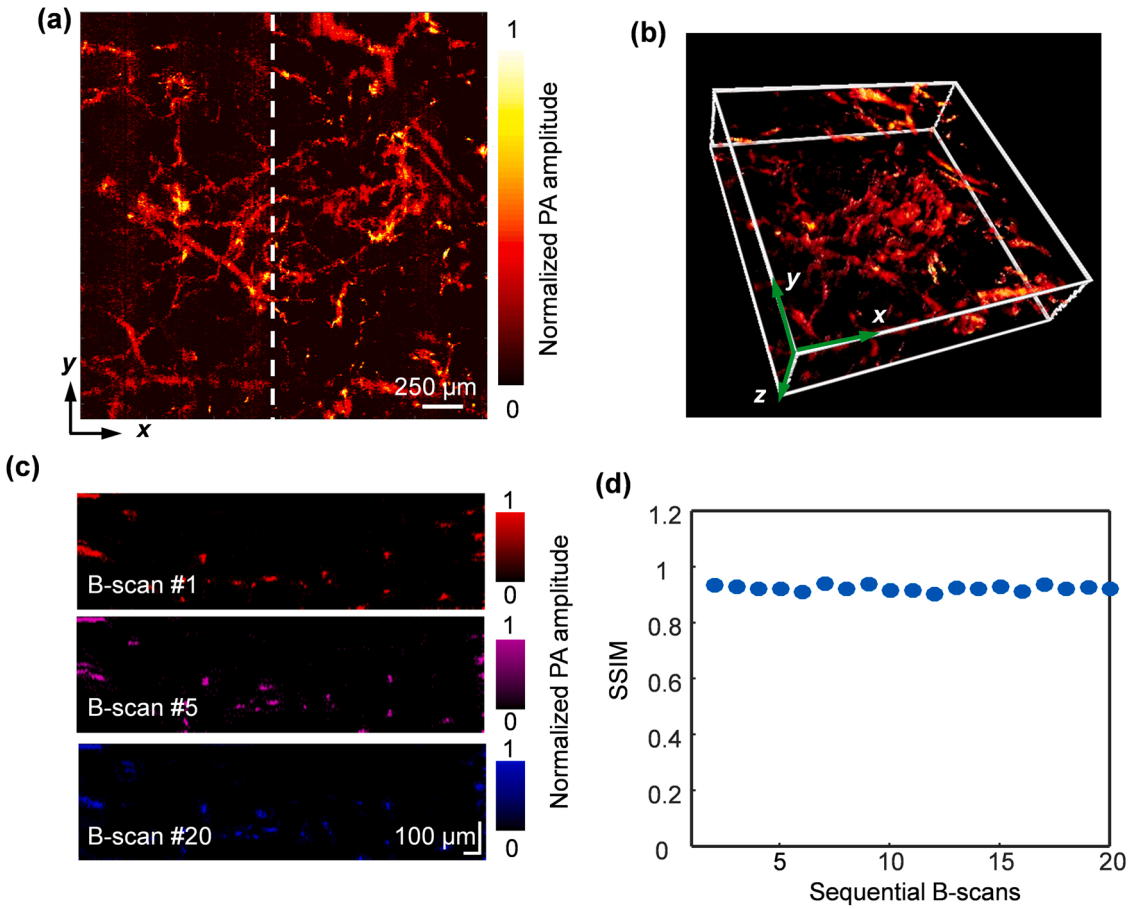

Fig. 6. Maximum-amplitude-projection (a) and volumetric views (b) of microvessels of a mouse ear in vivo. Movie 3 (Supplementary materials) provides volumetric visualization of the microvessels. (c) Three repeated B-scan images from the same lateral position. Movie 4 (Supplementary materials) shows all cross-sectional microvascular images. (d) SSIMs between the first B-scan frame and subsequent each one. The lateral position of the B-scan images was approximately highlighted by the white dotted line in (a). PA: photoacoustic.

In this work, we developed a common-path interferometric SPR sensor for highly sensitive measurement of the broadband photoacoustic waves while stabilizing the signal output effectively. Encoding the photoacoustically-modulated phase shift (Fig. 1(b) and (d)) into the time-varying interferometric intensity (Fig. 1(e)), ultrasensitive photoacoustic measurement (~95.6-Pa NEP value) over the frequency bandwidth of ~173 MHz was achieved in this sensor, which was analogous to our recently-established phase-shifted SPR sensor [29]. Remarkably, the proposed sensor adopted one single incident beam as the interrogation light, in which the two orthogonally polarized components (i.e., *p*- and *s*-polarization) travelled through the common optical path. Such configuration permitted the initial phase difference (i.e., under zero ultrasonic pressure) being almost constant, so that the destabilization from the randomly fluctuating phase was eliminated (Fig. 1(e)). Consequently, the time-varying interferometric intensity solely encoded the photoacoustically-perturbed phase shift (Eq. 4). Ultrasensitive, broadband photoacoustic measurement is thereby accessed with excellent stability (Fig. 3(b-e)). Volumetric imaging of phantom (Fig. 5) and mouse ear in vivo (Fig. 6) was obtained using an OR-PAM system incorporating the common-path interferometric SPR sensor.

To reinforce biomedical photoacoustic investigations, further improvement is required in our OR-PAM system. Due to the ultrasonic detection at transmission mode, the applications are limited to thin biological samples, such as body extremities (e.g., mouse ears in Fig. 6). This drawback can be overcome using reflection-mode OR-PAM by configuring a miniature sensor within the central cone of a reflective objective [26], which accommodates to various biomedical imaging applications, including brain and eye [4,8,17,33], while does not compromise the sensitivity, bandwidth, or stability. With miniaturization of the sensor, photoacoustic endoscopic technology could incorporate our sensor instead of the piezoelectric transducer [34,35], potentially accessing volumetric visualizations with improved imaging contrast and depth resolution. Determined by 0.1-NA optical objective, the photoacoustic illumination has a short depth of focus. Our system possibly fails to excite the samples away from the focal zone, and the imaging is reconstructed with low contrast and compromised lateral resolution. Axially enlarging the depth of focus by wavefront engineering technologies allows uniform photoacoustic excitation at prolonged depth range [36–38], thus providing better volumetric visualizations. Monitoring the dynamic physiological processes within the biological tissues, such as treatment responses and brain functions [4,5,32], depends upon fast imaging acquisition in the photoacoustic microscopes. Instead of using slow scanning stages based on stepper motor, the integration of high-speed mirror scanner into the OR-PAM, such as galvanometer mirror, micro-electro-mechanical system (MEMS) scanner, or polygon-mirror scanner [39–42], could speed up the imaging capture, and the functional activities can thus be better understood.

In summary, by delicately configuring the interrogation light of the SPR sensing, ultrasensitive, broadband, and highly stable photoacoustic measurement is achieved in the OR-PAM system incorporating a common-path interferometric SPR sensor. Potentially, the novel sensing technology would be invaluable for a wide range of applications in the field of biomedical photoacoustic investigations.

Declaration of Competing Interest

The authors declare no conflicts of interest.

Data Availability

Data will be made available on request.

Acknowledgment

This work was supported in part by Guangdong Major Project of Basic and Applied Basic Research: 2020B0301030009; National Natural Science Foundation of China (NSFC): 61875130, 62175159, 62175157; Science and Technology Innovation Commission of Shenzhen: KQTD20170330110444030, JCYJ20200109113808048, RCJC20210609103232046; Key Research Project of Zhejiang Lab: K2022MG0AC05. W. Song appreciates the support from Shenzhen University: No. 860-000002110434. The authors would like to acknowledge the Photonics Center of Shenzhen University for technical support.

Appendix A. Supporting information

Supplementary data associated with this article can be found in the online version at doi:10.1016/j.pacs.2022.100419.

References

[1] L.V. Wang, S. Hu, Photoacoustic tomography: in vivo imaging from organelles to organs, Science 335 (2012) 1458–1462.
[2] L.V. Wang, J. Yao, A Practical guide to photoacoustic tomography in the life sciences, Nat. Methods 13 (2016) 627–637.
[3] C. Liu, J. Chen, Y. Zhang, J. Zhu, L. Wang, Five-wavelength optical-resolution photoacoustic microscopy of blood and lymphatic vessels, Adv. Photon. 3 (2021), 016002.
[4] W. Song, Q. Wei, W. Liu, T. Liu, J. Yi, N. Sheibani, A. Fawzi, R.A. Linsenmeier, S. Jiao, H.F. Zhang, A combined method to quantify the retinal metabolic rate of oxygen using photoacoustic ophthalmoscopy, Sci. Rep. 4 (2014) 6525.
[5] T. Jin, W. Qi, X. Liang, H. Guo, Q. Liu, L. Xi, Photoacoustic imaging of brain functions: wide filed-of-view functional imaging with high spatiotemporal resolution, Laser Photonics Rev. 16 (2022), 2100304.
[6] A. Ron, X.L. Deán-Ben, S. Gottschalk, D. Razansky, Volumetric optoacoustic imaging unveils high-resolution patterns of acute and cyclic hypoxia in a murine model of breast cancer, Cancer Res 79 (2019) 4767–4775.
[7] J. Shi, T.T.W. Wong, Y. He, L. Li, R. Zhang, C.S. Yung, J. Hwang, K. Maslov, L. V. Wang, High-resolution, high-contrast mid-infrared imaging of fresh biological samples with ultraviolet-localized photoacoustic microscopy, Nat. Photonics 13 (2019) 609–615.
[8] N.G. Horton, K. Wang, D. Kobat, C.G. Clark, F.W. Wise, C.B. Schaffer, C. Xu, *In vivo* three-photon microscopy of subcortical structures within an intact mouse brain, Nat. Photonics 7 (2013) 205–209.
[9] J. Yi, W. Liu, S. Chen, V. Backman, N. Sheibani, C. Sorenson, A. Fawzi, R. A. Linsenmeier, H.F. Zhang, Visible light optical coherence tomography measures retinal oxygen metabolic response to systemic oxygenation, Light.: Sci. Appl. 4 (2015), e334.
[10] P. Fei, J. Nie, J. Lee, Y. Ding, S. Li, H. Zhang, M. Hagiwara, T. Yu, T. Segura, C. Ho, D. Zhu, T.K. Hsiai, Subvoxel light-sheet microscopy for high-resolution high-throughput volumetric imaging of large biomedical specimens, Adv. Photonics 1 (2019), 016002.
[11] Q. Zhou, S. Lau, D. Wu, K.K. Shung, Piezoelectric films for high frequency ultrasonic transducers in biomedical applications, Prog. Mater. Sci. 56 (2011) 139–174.
[12] B. Dong, C. Sun, H.F. Zhang, Optical detection of ultrasound in photoacoustic imaging, IEEE Trans. Biomed. Eng. 64 (2017) 4–15.
[13] G. Wissmeyer, Looking at sound: optoacoustics with all-optical ultrasound detection, Light.: Sci. Appl. 7 (2018) 53.
[14] J. Guggenheim, J. Li, T. Allen, R. Colchester, S. Noimark, O. Ogunlade, I. Parkin, I. Papakonstantinou, A. Desjardins, E. Zhang, P. Beard, Ultrasensitive plano-concave optical microresonators for ultrasound sensing, Nat. Photonics 11 (2017) 714–719.
[15] W.J. Westerveld, M. Mahmud-Ul-Hasan, R. Shnaiderman, V. Ntziachristos, X. Rottenberg, S. Severi, V. Rochus, Sensitive, small, broadband and scalable optomechanical ultrasound sensor in silicon photonics, Nat. Photonics 15 (2021) 341–345.
[16] R. Shnaiderman, G. Wissmeyer, M. Seeger, D. Soliman, H. Estrada, D. Razansky, A. Rosenthal, V. Ntziachristos, Fiber interferometer for hybrid optical and optoacoustic intravital microscopy, Optica 4 (2017) 1180–1187.
[17] H. Li, B. Dong, X. Zhang, X. Shu, X. Cheng, R. Hai, D. Czaplewski, H.F. Zhang, C. Sun, Disposable ultrasound-sensing chronic cranial window by soft nanoimprinting lithography, Nat. Comm. 10 (2019) 4277.
[18] H. Li, B. Dong, Z. Zhang, H.F. Zhang, C. Sun, A transparent broadband ultrasonic detector based on an optical micro-ring resonator for photoacoustic microscopy, Sci. Rep. 4 (2014) 4496.
[19] R. Shnaiderman, G. Wissmeyer, O. Ülgen, Q. Mustafa, A. Chmyrov, V. Ntziachristos, A submicrometre silicon-on-insulator resonator for ultrasound detection, Nature 585 (2020) 372–378.
[20] Z. Fang, X. Zhu, Plasmonics in nanostructures, Adv. Mater. 25 (2013) 3840.
[21] S.G. Nelson, K.S. Johnston, S.S. Yee, High sensitivity surface plasmon resonance sensor based on phase detection, Sens. Actuators B 35 (1996) 187.
[22] C. Zhang, R. Wang, C. Min, S. Zhu, X. Yuan, Experimental approach to the microscopic phase-sensitive surface plasmon resonance biosensor, Appl. Phys. Lett. 102 (2013), 011114.
[23] H.P. Ho, W.W. Lam, S.Y. Wu, Surface plasmon resonance sensor based on the measurement of differential phase, Rev. Sci. Instrum. 73 (2002) 3534–3539.
[24] R. Nuster, G. Paltauf, P. Burgholzer, Comparison of surface plasmon resonance devices for acoustic wave detection in liquid, Opt. Express 15 (2007) 6087.
[25] T. Wang, R. Cao, B. Ning, A. Dixon, J. Hossack, A. Klibanov, Q. Zhou, A. Wang, S. Hu, All-optical photoacoustic microscopy based on plasmonic detection of broadband ultrasound, Appl. Phys. Lett. 107 (2015), 153702..
[26] W. Song, L. Peng, G. Guo, F. Yang, Y. Zhu, C. Zhang, C. Min, H. Fang, S. Zhu, X. Yuan, Isometrically resolved photoacoustic microscopy based on broadband surface plasmon resonance ultrasound sensing, ACS Appl. Mater. Interfaces 11 (2019) 27378–27385.
[27] W. Song, S. Xiao, C. Min, H. Fang, X. Yuan, Theoretical and experimental studies on broadband photoacoustic response of surface plasmon sensing, Appl. Phys. Lett. 116 (2020), 243504.
[28] V.V. Temnov, C. Klieber, K.A. Nelson, T. Thomay, V. Knittel, A. Leitenstorfer, D. Makarov, M. Albrecht, R. Bratschitsch, Femtosecond nonlinear ultrasonics in gold probed with ultrashort surface plasmons, Nat. Commun. 4 (2013) 1468.
[29] F. Yang, W. Song, C. Zhang, H. Fang, C. Min, X. Yuan, A phase-shifted surface plasmon resonance sensor for simultaneous photoacoustic volumetric imaging and spectroscopic analysis, ACS Sens. 6 (2021) 1840–1848.
[30] Z. Wang, A.C. Bovik, H.R. Sheikh, E.P. Simoncelli, Image quality assessment: from error visibility to structural similarity, IEEE T Image Process 13 (2004) 600–612.
[31] G. Ku, K. Maslov, L. Li, L.V. Wang, Photoacoustic microscopy with 2-microm transverse resolution, J. Biomed. Opt. 15 (2010), 021302.
[32] Y. He, L. Wang, J. Shi, J. Yao, L. Li, R. Zhang, C. Huang, J. Zou, L.V. Wang, *In vivo* label-free photoacoustic flow cytography and on-the-spot laser killing of single circulating melanoma cells, Sci. Rep. 6 (2016) 39616.
[33] H. Zhao, K. Li, F. Yang, W. Zhou, N. Chen, L. Song, C. Zheng, Z. Liu, C. Liu, Customized anterior segment photoacoustic imaging for ophthalmic burn evaluation in vivo, Opto-Electron Adv. 4 (2021), 200017.
[34] Y. Li, R. Lin, C. Liu, J. Chen, H. Liu, R. Zheng, X. Gong, L. Song, *In vivo* photoacoustic/ultrasonic dual-modality endoscopy with a miniaturized full field-of-view catheter, J. Biophoton. 11 (2018), e201800034.
[35] J. Zhang, M. Du, J. Fang, S. Lv, W. Lou, Z. Xie, Z. Chen, X. Gong, *In vivo* evaluation of endometrium through dual-modality intrauterine endoscopy, Biomed. Opt. Express 13 (2022) 2554–2565.
[36] J. Shi, L. Wang, C. Noordam, L.V. Wang, Bessel-beam grueneisen relaxation photoacoustic microscopy with extended depth of field, J. Biomed. Opt. 20 (2015), 116002.
[37] B. Jiang, X. Yang, Q. Luo, Reflection-mode bessel-beam photoacoustic microscopy for in vivo imaging of cerebral capillaries, Opt. Express 24 (2016) 20167–20176.
[38] W. Song, Y. Wu, Y. Gao, T. Chen, W. Zheng, H. Fang, L. Song, X. Yuan, Flexibly adjustable depth-of-focus photoacoustic microscopy with spatial light modulation, Appl. Phys. Lett. 113 (2018) 16.
[39] B. Lan, W. Liu, Y. Wang, J. Shi, Y. Li, S. Xu, H. Sheng, Q. Zhou, J. Zou, U. Hoffmann, W. Yang, J. Yao, High-speed widefield photoacoustic microscopy of small-animal hemodynamics, Biomed. Opt. Express 9 (2018) 4689–4701.
[40] F. Yang, G. Guo, S. Zheng, H. Fang, C. Min, W. Song, X. Yuan, Broadband surface plasmon resonance sensor for fast spectroscopic photoacoustic microscopy, Photoacoustics 24 (2021), 100305.
[41] J.W. Baik, J.Y. Kim, S. Cho, S. Choi, J. Kim, C. Kim, Super wide-field photoacoustic microscopy of animals and humans in vivo, IEEE Trans. Med. Imaging 39 (2019) 975–984.
[42] K. Wang, C. Li, R. Chen, J. Shi, Recent advances in high-speed photoacoustic microscopy, Photoacoustics 24 (2021), 100294 (…).

Wei Song received his Ph.D. degree from Harbin Institute of Technology, Harbin, China, in 2014. He was an assistant professor with Shenzhen Institute of Advanced Technology from 2015 to 2016. Since 2017, he works as an assistant professor at Nanophotonics Research Centre, Shenzhen University. His main interest is the development and application of novel optical sensing and imaging technologies, including optical surface wave sensing, photoacoustic microscopy, and multimodal imaging.

Yushu Dong obtained her Bachelor degree from Shenzhen University in 2019. He is currently a Master student of Shenzhen University. His research interests include optical sensing and photoacoustic imaging.

Youxian Shan is a Ph.D. candidate at College of Physics and Optoelectronic Engineering, Shenzhen University. He received Bachelor degree from the Datong University in 2016, and received M.S. degree from Shenzhen University in 2020. His research focuses on the development of novel photoacoustic imaging technologies.

Fan Yang is a postdoctoral researcher at Nanophotonics Research Centre, Shenzhen University. He received his Ph.D. degree from College of Physics and Optoelectronic Engineering, Shenzhen University. His research focuses on the development of novel photoacoustic imaging technologies.

Changjun Min received his B.S. degree and Ph.D. degree from University of Science and Technology of China in 2003 and 2008, respectively. During 2008–2011 he was a postdoctoral research fellow in Louisiana State University (USA) and then in Nanyang Technological University (Singapore). During 2011–2014, he worked as Associate Professor in Nankai University (China). Since June 2014, he joined the College of Optoelectronic Engineering in Shenzhen University (China). His research interests include plasmonics, optical sensing/imaging, optical tweezers, vector beams, and metasurface. He has published over 100 journal papers in optics and photonics.

Xiaocong Yuan received BEng and MEng degrees in Optical Engineering from Tianjin University, China, in 1985 and 1988, respectively, and Ph.D. degree in Physics from the University of London, King's College, in 1994. Between 1994 and 1999, he was a research fellow with the Cavendish Laboratory, the University of Cambridge. Between 1999 and 2008, he was a faculty (tenured) in the School of EEE of Nanyang Technological University, Singapore. He joined the Institute of Modern Optics of Nankai University as a Chang Jiang distinguished professor in 2008. He relocated to Shenzhen University in 2013 to found the Nanophotonics Research Centre. His current work deals with optical vortices and applications, optical trapping, plasmonics in microscopy, and optical communication with orbital angular momentum. He has published more than 260 journal papers in optics and photonics. He is a SPIE and OSA Fellow.